Istraživanja i projektovanja za privredu
ISSN 1451-4117
DOI:10.5937/jaes0-67281
www.engineeringscience.rs

iipp publishing

Journal of Applied Engineering Science
Original Scientific Paper,
Volume 24, Number 4, Year 2026,
no 1366, pp 715-729

EXPERIMENTAL AND ANALYTICAL INVESTIGATION OF TIRE–CONCRETE INTERACTION CONSIDERING PERFORMANCE PARAMETERS

Swapnil Shinde[1]*, Dhananjay Khankal[1], Ashok Tadamalle[2], Sagar Deokar[3], Gaurav Dave[3], Sidheshwari Devkar[4]

[1]Savitribai Phule Pune University, Sinhgad College of Engineering, Department of Mechanical Engineering, Pune, India
[2]Shri Vile Parle Kelavani Mandal's Dwarkadas J. Sanghvi College of Engineering, Department of Mechanical Engineering, Mumbai, India
[3]Savitribai Phule Pune University, Sinhgad Technical Education Society's Smt. Kashibai Navale College of Engineering, Department of Mechanical Engineering, Pune, India
[4]Savitribai Phule Pune University, Sinhgad Technical Education Society's Smt. Kashibai Navale College of Engineering, Department of Computer Engineering, Pune, Maharashtra, India
**swapnil.shinde.sit@sinhgad.edu*

Tire–road interaction governs vehicle traction, directional stability, energy dissipation, and thermal behaviour; however, the coupled effects of operating conditions on mechanical, thermal, and pneumatic responses remain difficult to quantify experimentally. This study presents a controlled experimental and analytical investigation of localized tire–concrete interaction using a purpose-built test rig. A 195/65 R15 pneumatic tire was tested against a 400 mm diameter and 50 mm-wide concrete wheels under normal loads of 500, 1000, and 1500 N, rotational speeds of 50–400 rpm and slip angles of 0–20°. The full-factorial experimental design comprised 225 operating conditions and 675 individual runs with triplicate repetition. Frictional torque, infrared surface temperature, embedded subsurface temperature, and tire cavity pressure were simultaneously monitored to characterize the coupled response. Frictional torque increased predominantly with normal load and slip angle, while frictional power and temperature rise exhibited stronger dependence on rotational speed. A reduced-order analytical framework integrating Coulomb friction, frictional-energy dissipation, lumped-capacitance thermal modelling, and an ideal-gas-based pressure relation was evaluated against experimental measurements. Model predictions achieved values of 0.95, 0.93, 0.96, 0.92, 0.87, and 0.90 for frictional torque, apparent friction coefficient, frictional power, surface temperature, internal temperature, and cavity pressure, respectively. The framework effectively captures the principal coupled response trends within the investigated operating domain. The findings support comparative assessment of localized tire–concrete thermo-mechanical-pneumatic behaviour and are interpreted as physical-regime trends rather than direct full-scale tire–road predictions because of the finite curvature and restricted width of the laboratory contact surface.

Keywords: tire road interaction, slip angle, frictional torque, thermal response, tire pressure variation, energy dissipation, experimental modelling

HIGHLIGHTS

- Experimental and Thermo-Mechanical Investigation of Tire–Concrete Frictional Contact Under Variable Slip Conditions
- Energy-Based Modelling and Experimental Analysis of Tire–Road Interaction Considering Frictional Heating and Slip Dynamics
- Thermo-Mechanical Behaviour of Tire–Concrete Contact: Experimental Evaluation of Friction, Heat Generation, and Pressure Variation.

1 Introduction

The tire–road interface constitutes the primary mechanical pathway through which traction, braking, and cornering forces are transmitted between a vehicle and the road surface. Its behaviour therefore directly influences vehicle safety, directional stability, rolling resistance, energy consumption, and tire durability. Despite its practical importance, tire–road contact remains a complex tribological system because local asperity interactions, tread deformation, carcass response, frictional sliding, and heat transfer occur simultaneously over substantially different spatial and temporal scales. Classical tire dynamics, including the formulation established by Pacejka [1-3], relates longitudinal and lateral forces principally to slip ratio and slip angle, respectively. Within a given contact regime, tangential frictional force generally increases with normal load, whereas the apparent coefficient of friction may exhibit a comparatively weaker load dependence. In contrast, the rate of frictional energy dissipation is strongly influenced by relative motion at the interface. Experimental investigations [4,6] have demonstrated that energy loss can vary

considerably with operating speed even when changes in apparent friction coefficient remain comparatively limited, making speed an important parameter governing thermal loading during sustained operation. Thermo-mechanical models incorporating frictional heat generation, conduction, and convection have consequently been developed to describe these coupled processes [7,8]. Infrared thermography has also become an important experimental technique for identifying surface-temperature distributions and localized thermal hotspots. Nevertheless, mechanical, thermal, and pneumatic responses are frequently investigated separately or using only a limited combination of sensing modalities, restricting direct assessment of their coupled evolution under systematically controlled operating conditions [9].

In addition to performance and safety, tire-road friction results in the emission of particulate matter -tire-wear particles (TWP) whose environmental and public-health effects are under the focus of current intense scrutiny [10-12]. Mass loss rate is proportional to cumulative frictional energy input, which is why energy dissipation is a measurement of the important output of mechanical and thermal variables. The classical tire mechanics determines the slip angle to be the main variable that constrains the lateral traction. Pacejka [1] gave the empirical "Magic Formula" between lateral force and slip angle: low-angle behaviour (low angle) is determined by the initial slope (cornering stiffness) and the maximum coefficient of friction and its subsequent saturation by the high-angle regime. The longitudinal analogue - force versus slip ratio - is qualitatively similar. The basic mechanics of contact were developed by Bowden and Tabor [13]: friction is the result of adhesion as well as deformation (ploughing) components, and on clean smooth surfaces like those considered here adhesion predominates.

Alternative developments of intelligent tire systems in the recent past have expanded the classical framework to real-time estimation. Gu [2] suggested a new friction sensor of the tire-road interaction on piezoelectric tire signals. Dong et al. [3] designed a lateral stability controller of distributed-drive electric vehicle, which uses real-time estimates of the slip-angle, which proves to be a practical application of friction models in vehicle control. Zhao et al. [4] gave an adaptive estimation combined with machine-learning post-processing of the tire-road friction coefficient through intelligent tire signals, and the results were real-time performance at advanced driver assistance system (ADAS) level. The definitions of rolling resistance and rolling loss were revisited by Biffi et al. [5] who tested both theoretically and experimentally, on a flat-road roller bench, and found that the rate of energy dissipation increased proportionally with speed even with a quasi-constant apparent coefficient of friction. This causes speed to be a significant secondary variable of thermal loading- a phenomenon that is repeated in the current experiments (see Figs. 4 and 10). Mujdeci et al. [6] used finite-element modelling on tire fatigue, and this indicated that internal heat was produced through cyclic deformation under combined slip and load, and the heat accumulated in the tire body during prolonged testing. The heat at the contact patch is divided between the tire tread, the road substrate and the air within the enclosure. The fraction of partition is a factor which is dependent on the thermal properties of each component as well as the geometry of the component. The standard framework of conductivity, convection and radiation in solids is given by Incropera and DeWitt [7], their lumped-capacitance model (when the $Bi = hL/k$ratio is less than 0.1) is the foundation of the thermal model in Section 4. Stefanelli et al. [8] have created a unified thermomechanical modelling of tires systems and brake systems in the dynamics and safety of vehicles and shown that joint thermal-mechanical modelling is necessary to forecast contact temperatures during combined braking and cornering. The infrared thermal imaging was tested and confirmed to be the reliable non-invasive approach to monitor the operating temperatures on tires and wheels, and Li et al. [9] confirmed that the surface hot-spots are effective proxies to measure the subsurface heat generation under moderate thermal gradients. Tire-wear particles (TWP) and airborne particulate emissions are formed by tire-road friction, which have recently become the subject of significant regulatory and scientific concern. Papaioannou et al. [10] researched the wear-emission reduction strategies of automated articulated vehicles and demonstrated that slip could be controlled in real-time and decreases emissions substantially. Beji et al. [11] described the physical and chemical behavior of TWP and found that the morphology and composition of the particles are highly dependent on the frictional energy input per unit area, i.e. the power density $\Pi = Pfric/A$. M Muller et al. [12] reviewed the emissions of the using tire phase and found driving conditions in terms of slip, load and speed to be the key determinants The results encourage the measurement of cumulative frictional energy as an important experimental product as in Section 4.3.

The above review indicates that three gaps are not fully covered by the current literature: (i) multi-sensor data at a time, combining torque, full-field IR temperature, embed temperature and tire pressure across a systematic parameter matrix at multiple depths and at multiple depths; (ii) explicit analyses of the energy-balance relating frictional power input to experimentally measured thermal uptake and pressure rise within the wheel-tire system, along with The current work satisfies the three gaps. Recent investigations have progressively combined mechanical, thermal, imaging, and intelligent-tire measurements to characterize tire–road interaction; however, the sensing configurations and investigated operating variables differ considerably among studies. Comparatively limited experimental work has simultaneously integrated frictional torque, full-field infrared surface temperature, embedded subsurface temperature, and tire cavity pressure within a single controlled test platform while systematically varying slip angle, normal load, and rotational speed. The novelty of the present study therefore does not arise from the individual sensing techniques themselves, but from their coordinated application within a full-factorial experimental framework and their subsequent integration into a physically interpretable thermo-mechanical–pneumatic model.

2 Materials and methods

2.1 Test rig design and layout

A purpose-built tire–concrete interaction test rig was developed to permit independent control of normal load, concrete-wheel rotational speed, and tire slip angle. The complete experimental facility is shown photographically in Fig. 1, while the geometric arrangement and instrumentation locations are presented schematically in Fig. 2. The rig comprises four principal subsystems: the drive unit, concrete-wheel and shaft assembly, tire positioning/slip-angle mechanism, and normal-load application system. The concrete test wheel, 400 mm in diameter and 50 mm in thickness, was mounted on a rigid steel shaft supported by a self-aligning bearing arrangement. The shaft was driven by a variable-frequency-drive-controlled three-phase induction motor rated at 2.2 kW and 1450 rpm through a reduction gearbox, permitting controlled wheel speeds from 50 to 400 rpm. A strain-gauge torque transducer was installed in-line with the wheel shaft to measure the resisting torque generated at the tire–concrete interface. The pneumatic tire was mounted on a rigid sub-frame incorporating a precision worm-gear angular adjustment mechanism. This arrangement permitted the tire orientation relative to the wheel direction of motion to be varied through slip angles of 0°, 5°, 10°, 15°, and 20°, with an angular positioning accuracy of ±0.1°. Normal loads of 500, 1000, and 1500 N were applied vertically through a calibrated dead-weight loading arrangement. As illustrated in Fig. 2, three Type-K thermocouples were embedded in the concrete wheel at depths of 5, 15, and 30 mm below the running surface to characterize subsurface thermal penetration. The IR thermal camera was positioned approximately 0.35 m from the contact region at a viewing angle of 45° to obtain full-field surface-temperature measurements.

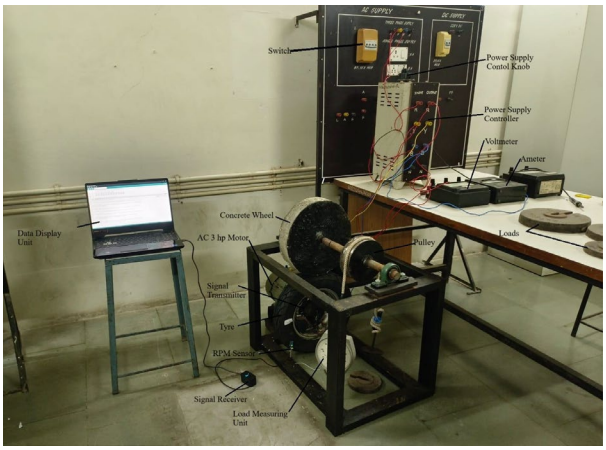

Fig. 1. Experimental test setup photograph

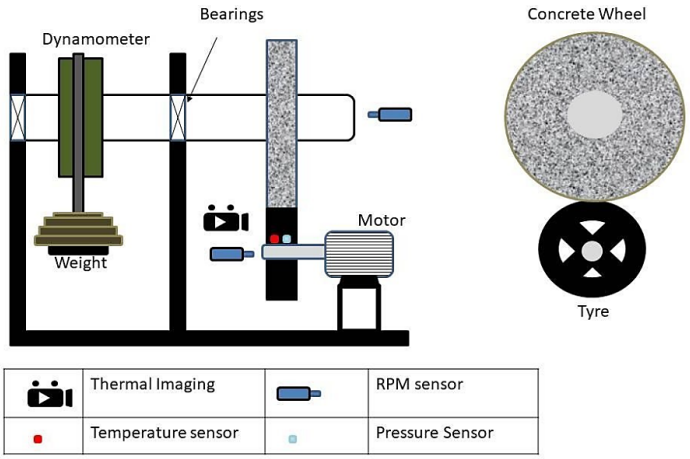

Fig. 2. Schematic diagram of the test setup

2.2 Test materials

Concrete Test Wheel — A reinforced concrete disc of 400 mm diameter and 50 mm thickness was cast from ordinary Portland cement (Grade M35; water–cement ratio w/c = 0.40) and cured for 28 days under standard moist conditions. After curing, the running surface was ground to a consistent finish. Surface roughness was measured at five uniformly distributed locations using a calibrated stylus profilometer (ISO 4287): mean Ra = 1.25 μm, Rz = 8.4 μm. Concrete was selected because of its high compressive strength (fccube = 35 MPa), well-characterised thermal properties (specific heat c = 880 J/ kg K; thermal conductivity k = 1.6 W/ m K [13, 14]) and its ability to absorb and dissipate frictional heat effectively, making it suitable for extended contact experiments without rapid degradation of the road-surface surrogate. Tire Specimen — A standard light-vehicle pneumatic tire (nominal size 195/65 R15, load index 91, speed index H) was used throughout. The tire was inflated to 200 kPa cold before each test condition. The rubber compound is of a typical passenger-car formulation, representative of the majority of vehicles for which tire–road interaction data are required [14]. Contact area between the tire and the concrete wheel was measured using pressure-sensitive film (Fuji Prescale, medium grade) at each load level and digitised by image analysis: 18–22 cm² at 500 N; 28–32 cm² at 1000 N; 38–43 cm² at 1500 N. The mean contact pressure at 1000 N is ≈ 0.33 MPa, well within the dry rigid-contact regime where Coulomb's law is applicable and the contact area is approximately elliptical (consistent with Hertzian contact theory [14]). The test tire was designated 195/65 R15, for which 195 mm represents the nominal section width rather than the measured tread-contact width. Therefore, this value should not be interpreted directly as the effective contact width. In comparison, the concrete wheel provides a 50 mm-wide running surface, resulting in contact with only a localized transverse portion of the tire tread. Consequently, the experimental configuration does not reproduce the complete full-width footprint, including both tire shoulders. Instrumentation

The instrumentation package was developed to record all the key variables in simultaneous, synchronised records at a resolution low enough to determine both quasi-steady trends and transient responses during the speed ramp-up. All instruments with their measurement ranges, resolutions and expanded uncertainties (k = 2, 95% confidence level) are summarised in table 1. A full-bridge strain-gauge transducer with a 50 Nm rating and a 0.05 Nm resolution was connected in-line to the concrete-wheel shaft and connected its output through the slip-ring assembly to the

DAQ. Three Type-K thermocouples were placed in the concrete disc at radial depths of 5, 15 and 30 mm below the running surface; the multi-depth device enables the characterisation of the temperature gradient in the subsurface and the data obtained can be used to verify the lumped-capacitance thermal model. The IR thermal camera was mounted at a standoff distance of 0.35 m and incidence angle of 45º; the emissivity of the concrete surface was measured to be 0.92 with the help of a calibrated blackbody reference source. Prior to the experimental campaign, the apparent emissivity of the concrete running surface was established using a calibrated blackbody reference. The camera was first aligned with the reference source under controlled viewing conditions and subsequently directed toward the concrete surface while the emissive setting was adjusted until the indicated infrared temperature agreed with the independently established reference temperature. The resulting surface emissivity was, which was used for all subsequent thermal measurements. The infrared camera was further verified against the calibrated blackbody at nominal temperatures of 30, 50, and 70 °C, and the corresponding correction values were incorporated into the data-processing procedure. During the tire–concrete experiments, the camera was maintained at a standoff distance of approximately 0.35 m and a viewing angle of 45°.

Table 1. Instrumentation specifications: sensors, measurement ranges, resolutions and expanded uncertainties

Instrument / Sensor	Measurement Range	Resolution	Uncertainty (k=2)
Strain-gauge torque sensor (full Wheatstone bridge)	0–50 N·m	0.05 N·m	±0.34 N·m (±2.1% FS)
Optical tachometer (reflective strip, non-contact)	0–3000 rpm	1 rpm	±2 rpm
Type-K thermocouples × 3 (embedded at 5, 15 and 30 mm depth)	−40 to 1200 ºC	0.1 ºC	±2.2 °C (per ASTM E230)
IR thermal camera (FLIR A-series; surface emissivity ε = 0.92)	−20 to 350 ºC	0.05 ºC	±2 °C or ±2% rdg
Piezoresistive pressure transducer	0–600 kPa	0.5 kPa	±1.2 kPa (±0.35% FS)
16-channel DAQ system (NI USB-6211 or equivalent)	±10 V, 16-bit ADC	0.3 mV	0.003% FS

2.3 Experimental procedure

Sensor Calibration — All sensors were calibrated to independent, traceable standards before all experimental runs. Calibration OIML Class M1 calibration masses were placed on the torque sensor at a known lever arm [15]; the calibration was done at five points over the 030 Nm operating range. The thermocouples were tested at the ice point (0 ºC, crushed ice/water slurry) and the steam point (100 ºC, boiling distilled water at the local atmospheric pressure) according to ASTM E230 [16]. Five levels of pressure were compared to the pressure transducer with a certified digital reference manometer (±0.1 kPa) in table 2. The IR camera was tested with a calibrated blackbody at 30 ºC, 50 ºC and 70 ºC; the corrections were made as a look up table in the DAQ software.

Table 2. Full-factorial test matrix: parameter levels, replication strategy and total number of runs

Parameter	Values / Range	No. of Discrete Levels
Normal Load	500 N, 1000 N, 1500 N	3
Rotational Speed	50–400 rpm (step 25 rpm)	15
Slip Angle	0°, 5°, 10°, 15°, 20°	5
Tire Inflation Pressure	200 kPa (cold, before each run)	1 (monitored continuously)
Test Duration per Condition	300 s (steady-state phase)	—
Replication	3 repetitions per condition	—

Test Execution- Each test condition was conducted in the following way. (i) The tire was attached to the specimen holder and inflated to 200 kPa; the angular position of the tire was adjusted to the desired slip angle. (ii) Dead-weights were used to apply the prescribed normal load. (iii) VFD control was used to start the motor and ramp it to the target speed; the DAQ started recording all the channels at the same time at 50 Hz at t = 0. (iv) The test was run for 300 s. The initial 60 s is generally associated with warm-up and thermal transient; and the last 60 s of each run were steady-state averaging. (v) The motor was then stopped at the end of each test and the wheel and tire allowed to cool naturally to a temperature of within 2 ºC of ambient temperature before the next condition. Each condition was done thrice on different days to record between-day variation; values are reported as arithmetic means and error bars on all figures are the standard deviation of 3 replicates.

2.4 Measurement uncertainty analysis

Measurement uncertainty was assessed according to the GUM framework (ISO/IEC Guide 98-3 [17]) with Type-A statistical uncertainty (standard deviation of three replicates divided by 93) and Type-B instrument-specification uncertainty added in quadrature to obtain the overall standard uncertainty u c. The increased uncertainty U = k u c with a coverage factor k = 2 which represents about 95 percent coverage of a normal distribution. The complete uncertainty budget of each measurand, along with the most important source of uncertainty, is shown in Table 3. The total experimental error in the determined coefficient of friction μ was 0.008, and in frictional power P fric was 0.082 (expanded, k 2), both within reasonable ranges of tribological experiments of this nature. Use the following uncertainty expression:

$$u_{T_s} = \sqrt{u_{cam}^2 + u_{\varepsilon}^2 + u_{rep}^2}$$

where u_{Ts} is the combined standard uncertainty of the surface-temperature measurement, ucam is the IR-camera calibration/specification contribution, u_{rep} is the emissivity-related contribution, and is the contribution associated with experimental repeatability. The combined uncertainty associated with infrared surface-temperature measurement was evaluated by considering the camera calibration/specification, emissivity-setting contribution, and run-to-run repeatability. These independent contributions were combined by the root-sum-of-squares method. The expanded uncertainty was subsequently calculated using a coverage factor k=2, corresponding approximately to a 95% confidence level. The resulting expanded uncertainty of the surface-temperature measurement was approximately ±4.2 °C, consistent with the uncertainty budget reported in Table 3.

Table 3. Measurement uncertainty budget evaluated per ISO/IEC Guide 98-3 (GUM framework); k = 2, 95% confidence level

Measurand	u_A (Type-A)	u_B (Type-B)	u_c (combined)	U (k=2, 95%)
Torque (N·m)	±0.08	±0.15	±0.17	±0.34
Surface temperature (°C)	±0.6	±2.0	±2.09	±4.2
Internal temperature (°C)	±0.4	±1.0	±1.08	±2.2
Tire pressure (kPa)	±0.3	±0.5	±0.58	±1.2
Friction coefficient μ	—	—	±0.004	±0.008
Frictional power P_fric (W)	—	—	±4.1%	±8.2%

2.5 Surface roughness and contact area characterization

Surface roughness of the concrete wheel was measured using a stylus profilometer and measured value of average roughness *Ra* =1.25 μm. Contact area between Tire and wheel was estimated using pressure sensitive film. At 1000 N load the effective contact patch was 28 to32 cm². With dry, rigid contact and moderate surface roughness, Coulomb friction law is applicable that supporting Eq. (2). The effective tire–concrete contact area was measured using pressure-sensitive film positioned directly between the tire tread and concrete running surface under the prescribed normal load. After loading, the developed film was examined to identify the loaded footprint and determine its effective area. Representative contact-footprint images at 500, 1000, and 1500 N are presented in Fig. 4. The measured effective contact areas were approximately 18–22 cm², 28–32 cm², and 38–43 cm², respectively. Because the concrete running surface is limited to 50 mm in width, the pressure-film patterns should also be examined for contact reaching the transverse wheel boundaries. Any such boundary interaction is treated as an experimental geometric limitation rather than representative full-width tire behaviour.

2.6 Mathematical modelling

A system of closed-form analytical relations is established to explain the mechanical, energy and thermal behaviour of the tire-concrete system. The model is maintained in a deliberately parsimonious form - a single calibration parameter - to be an easy-to-use design tool and to reveal the underlying physical processes without being buried in numerical complexity.

2.7 Frictional torque and tangential contact force

The tangential frictional force at the tire–concrete interface was determined from the measured frictional torque using moment equilibrium about the concrete-wheel shaft:

$$T_f = F_f \cdot R \tag{1}$$

where $T_f(\mathrm{N\cdot m})$ is the measured frictional torque, $F_f(\mathrm{N})$ is the tangential contact force and R = 0.200 m is the effective rolling radius of the concrete disc. This relationship follows directly from the moment equilibrium of the wheel shaft.

2.8 Apparent coefficient of friction

Applying Coulomb's law of dry friction [18], in which the friction force is proportional to the normal load and independent of apparent contact area, the apparent coefficient of friction is:

$$\mu = F_f/N = T_f/(R \cdot N) \tag{2}$$

where N (N) is the applied normal load. Equation (2) is valid provided the contact remains in a single regime (adhesive or gross sliding). The near-constant μ–load relationship observed experimentally (Section 5.2) confirms this assumption. Note that μ as defined here is an apparent or effective coefficient that includes all dissipative mechanisms at the contact—adhesion, micro-ploughing and viscous losses—rather than the fundamental adhesion coefficient alone.

2.9 Slip ratio and slip angle

The longitudinal slip ratio s, characterising the relative sliding between the wheel periphery and the tire contact surface, is defined as [19]:

$$s = (v_w - v_t)/v_t \tag{3}$$

where v_w = ωR is the peripheral (tangential) speed of the rotating concrete disc and v_t is the tire tangential velocity. The geometric slip angle α relates to the lateral deformation of the tire carcass [20]:

$$tan\alpha = y/x \tag{4}$$

where y is the lateral (transverse) displacement of the contact point and x is the forward displacement. The slip angle α set by the angular fixture directly controls the lateral contact force and, through Eq. (2), the measured friction coefficient.

2.10 Frictional power dissipation

The mechanical power converted into heat at the contact patch is the product of the frictional torque and the angular velocity of the wheel [21]:

$$P_fric = T_f \cdot \omega \quad \text{where} \quad \omega = 2\pi N/60 rads^{-1} \tag{5}$$

Equation (5) is the standard power–torque–speed relation for rotating systems. Since torque T_f increases with slip angle (see Eq. (2)), and ω increases with rotational speed, frictional power is sensitive to both variables—explaining the steep rise in Figs. 4 and 10. At the most severe condition (1500 N, 400 rpm, 20° slip), Eq. (5) predicts $P_{fric} = T_f \times (2\pi \times 400/60) \approx 36.1 \times 41.9 \approx 1512$ W, in close agreement with the measured 1510 W.

2.11 Heat generation and temperature rise

The frictional power generated at the contact is distributed between the tire (absorbed by the rubber compound), the concrete wheel (absorbed by the near-surface layer) and the surroundings (convected and radiated from both surfaces). Denoting by η the fraction of the total power absorbed by the concrete wheel, the heat absorbed over a test duration t is:

$$Q = \eta \cdot P_{fric} \cdot t \tag{6}$$

The corresponding temperature rise of the thermally active concrete layer, treated as a lumped mass, is:

$$\Delta T = Q/(m \cdot c) \tag{7}$$

where m (kg) is the effective mass of the heated layer (estimated from the contact area and a penetration depth based on the thermal diffusivity and test duration) and c = 880 J/kg K is the specific heat capacity of concrete [22]. The applicability of the lumped-capacitance model requires the Biot number $Bi = hL/k$< 0.1. Taking h = 20 W/ m K

(natural convection), L = 5 mm (near-surface zone) and k = 1.6 W m⁻¹ K⁻¹, Bi ≈ 20 × 0.005 / 1.6 = 0.0625 < 0.1: the lumped approximation is justified.

2.12 Tire cavity pressure response

In the present reduced-order formulation, the temperature rise measured by the thermocouple located 5 mm below the contact surface, was used as an effective proxy for the thermal state associated with cavity-air heating. This approximation was adopted because a dedicated cavity-air temperature sensor was not incorporated into the present experimental configuration. Accordingly,

$$\Delta Tcavity \approx \Delta T5 \tag{8}$$

$$P/T = P_0/T_0 = constant$$

$$\Delta P = P_0 \cdot \Delta T_cavity/T_0 \tag{9}$$

where, P_0 is the initial tire cavity pressure and T_0 is the initial absolute temperature. The approximation does not imply that the subsurface concrete temperature and cavity-air temperature are physically identical; rather, $\Delta T5$ serves as an effective thermal-state variable in the simplified pressure model. Quantitatively, the resulting pressure predictions showed good agreement with the measured cavity pressure, with and RMSE ≈ 0.6 kPa across the experimental dataset. The approximation does not imply that the subsurface concrete temperature and cavity-air temperature are physically identical; rather, serves as an effective thermal-state variable in the simplified pressure model. Quantitatively, the resulting pressure predictions showed good agreement with the measured cavity pressure, with and RMSE ≈ 0.6 kPa across the experimental dataset. This agreement provides indirect validation at the pressure-response level, while direct validation of cavity-air temperature remains outside the scope of the present measurements [23].

2.13 Determination of the heat absorption fraction η

The heat-absorption fraction ηrepresents the proportion of frictional power absorbed by the thermally active concrete region. It was determined by inverse calibration at the mid-range condition of 1000 N normal load, 200 rpm rotational speed, and 10° slip angle. At this condition, the measured frictional power was P_{fric} = 280 W and the measured surface-temperature rise was $\Delta Ts = 18.3$ °C. Substitution of these values into Eqs. (6)–(7) yielded .. All predictions in Table 4 were made with this value constant; the consistency in the good fit (R2 = 0.87; maximum error = 5) over a six-fold range of frictional power P_{fric} is a testament to the fact that $\eta$is acceptably constant throughout the test matrix. Physically, η = 0.38, means that approximately 62% of the heat generated is absorbed in the tire and lost to the environment- reasonable since the thermal conductivity (Krubber = 0.25 W/mK) of rubber is much lower than concrete, limiting heat transfer into the wheel body.

2.14 Geometric sensitivity and scaling

The experimental rig was designed as a controlled tire–concrete contact simulator rather than a geometrically exact reproduction of a full-width tire operating on a flat pavement. The concrete wheel has a diameter of 400 mm, corresponding to a radius (Rw = 0.200) m, and a width of 50 mm. Consequently, the tire interacts with a localized concrete surface whose transverse extent is smaller than the complete tread width of the 195/65 R15 tire. This geometric constraint should be considered when interpreting the experimental results.

A first-order measure of curvature influence can be expressed using the wheel-to-tire curvature ratio,

$$\lambda_R = \frac{R_\omega}{R_t}$$

where R_ω is the concrete-wheel radius and R_t is the nominal unloaded tire radius. For the 195/65 R15 tire, the nominal outside diameter calculated from its dimensional designation is approximately 0.635 m, giving R_t = 0.317) m and hence λ_R=0.63). Therefore, the concrete surface cannot be regarded as locally identical to an infinite-radius flat pavement. Its convex curvature can modify the longitudinal extent and pressure distribution of the contact patch relative to flat-road contact. The second geometric consideration is the 50 mm wheel width. The experimentally measured contact areas increased from approximately 18–22 cm² at 500 N to 28–32 cm² at 1000 N and 38–43 cm² at 1500 N. These measurements demonstrate the expected increase in local contact area with normal load; however, the narrow wheel restricts lateral development of the complete tire footprint table 4. Accordingly, the setup does not reproduce the full transverse tread-pressure distribution, shoulder engagement, tread-pattern effects across the entire tire width, or global carcass deformation that occurs during full-width tire–road contact.

Table 4. Geometric sensitivity and applicability of the laboratory tire–concrete configuration

Geometric/Contact Parameter	Laboratory Configuration
Concrete wheel diameter	400 mm
Concrete wheel radius, (Rw)	200 mm
Nominal tire size	195/65 R15

Geometric/Contact Parameter	Laboratory Configuration
Nominal tire radius, (Rt)	317.25 mm
Wheel-to-tire curvature ratio, $(\lambda_R = R_w/R_t)$	0.63
Concrete wheel width	50 mm
Effective contact area at 500 N	18–22 cm²
Effective contact area at 1000 N	28–32 cm²
Effective contact area at 1500 N	38–43 cm²
Concrete surface roughness, (R_a)	1.25 µm
Biot number, (Bi)	≈ 0.063

The dimensionless quantities used in the present analysis should therefore be interpreted as indicators of physical-regime similarity rather than geometric equivalence. The measured friction number $\left(\Phi = F_f/N = \mu\right)$, imposed slip condition, contact power density $(\Pi = P_{\text{fric}}/A_{\text{contact}})$, and Biot number provide useful measures for comparing the dominant mechanical and thermal mechanisms. At the severe operating condition, the contact power density is of the order of $MWm(-2)$,while $(Bi \approx 0.063 < 0.1)$supports the lumped treatment of the thermally active layer. Thus, the rig is considered suitable for examining relative effects of slip angle, normal load, and rotational speed on localized frictional torque, energy dissipation, temperature rise, and pressure response under repeatable conditions. The measured absolute values should not, however, be interpreted as direct predictions of whole-tire performance on a flat road. Full-scale validation using a full-width road contact, large-radius drum, or instrumented vehicle test is required before quantitative extrapolation of the present results to complete tire behaviour.

3 Results and discussion

Results are presented in two groups. Section 5.1–5.5 examines the influence of slip angle (Figs. 3–8; data at 1000 N normal load unless otherwise stated) and Section 5.2–5.5 in parallel examines the influence of normal load (Figs. 9–14; data at 10° slip angle unless otherwise stated). Section 5.6 presents the model validation.

3.1 Frictional torque and friction coefficient — effect of slip angle and speed

Figure 3 illustrates the frictional torque versus rotational speed of all five slip angles at a constant normal load of 1000 N. At 0 o slip (pure rolling), the torque will increase with rotational speed, with the rolling-resistance torque increasing with speed as the viscoelastic energy dissipation in the tire body rises. At 400 rpm, the torque increases to about 4.5 N m due to the introduction of a 5º slip angle since the lateral force of contact is now contributing significantly to the total frictional force at the contact patch. The torque is increasing monotonically with slip angle: at 10, 15 and 20 slip the values of 400 rpm are about 7.2, 9.6 and 12.0 Nm. The ratio of $Tf(20)/Tf(0) = 5.7$at 400 rpm agrees with the Pacejka saturation behaviour of slip angles up to 20 and confirms that slip angle is the most significant control variable in torque generation. The roughly linear dependence of torque on speed of each constant slip angle is indicative of the quasi-Coulomb friction regime: as the speed rises, µ rises slightly with viscoelastic effects, increasing the friction force and, consequently, torque. Figure 4 shows the apparent coefficient of friction µ versus rotational speed of the slip-angle sweep. At 0 o slip, µ = 0.01 0.02 at all speeds, which indicates the low rolling-resistance force as compared with the normal force applied. The higher the slip angle (5, 10, 15 and 20 degrees), the faster µ increases: at 20 degrees slip, µ is 0.1214, almost 14 times higher than the pure-rolling value. This sharp rise is typical of the lateral-force saturation regime of the Pacejka model [1], in which the entire contact patch switches between partial sliding to gross sliding as the slip angle becomes larger than the peak. The almost load-independence of µ (Figs. 10) validates the Coulomb friction assumption and Equation (2): at 200 rpm and 10° slip, µ = 0.057 ± 0.003 at 500 N, 0.059 ± 0.004 at 1000 N and 0.061 ± 0.004 at 1500 N—variations well within the experimental uncertainty of ±0.008.

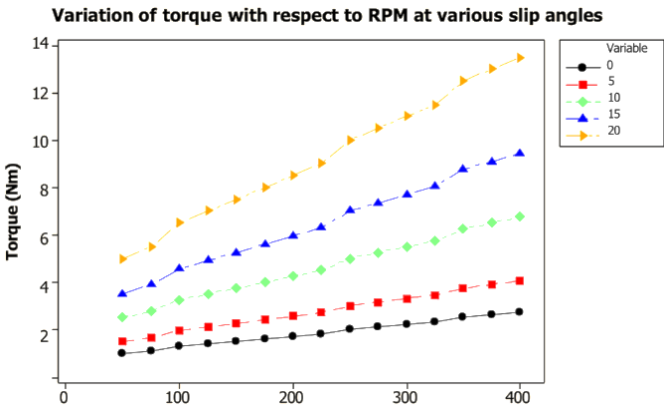

Fig. 3. Frictional torque versus rotational speed at five slip angles (0°–20°); normal load = 1000 N. Each data point is the mean of three replicates; error bars (±1 SD) are smaller than the symbols at most conditions

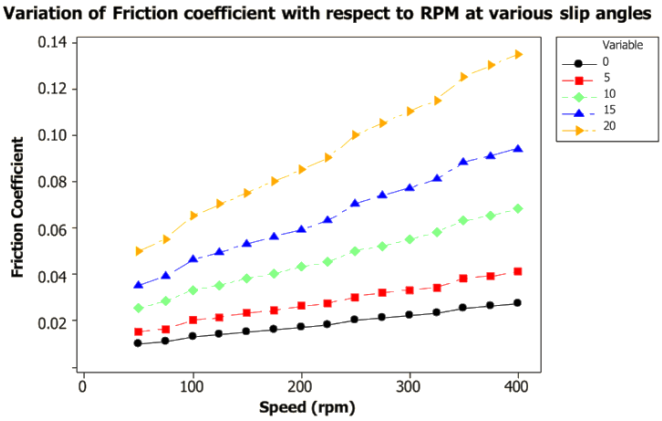

Fig. 4. Apparent coefficient of friction μ versus rotational speed at five slip angles (0°–20°); normal load = 1000 N. Slip angle, not speed or load, is the dominant determinant of μ

3.2 Frictional power dissipation

Figure 5 shows the frictional power P fric versus speed of the slip-angle sweep. Since $P_{fric} = T_f \omega$ (Eq. 5) and T f (via μ) and ω both depend on speed, power increases non-linearly, about the product of two functions that are monotonically increasing. P_{fric} is less than 100 W at 0º slip throughout the speed range, which implies that pure-rolling losses are small. At 5° slip, power reaches ≈ 185 W at 400 rpm. The increase accelerates with slip angle: at 20° slip and 400 rpm, P_{fric} exceeds 600 W (1000 N load, Fig. 4) and reaches ≈ 1510 W at 1500 N (Fig. 11). The large power input at combined high slip angle and high speed has two significant engineering consequences; first, it leads to rapid surface and internal heating (Sections 5.4 and 5.5), accelerating tire compound degradation; second, it is the cumulative energy input that causes tire-wear mass loss [11]. The data in Figs. 5 and 11 give a global view of the energy-dissipation landscape of the entire test matrix.

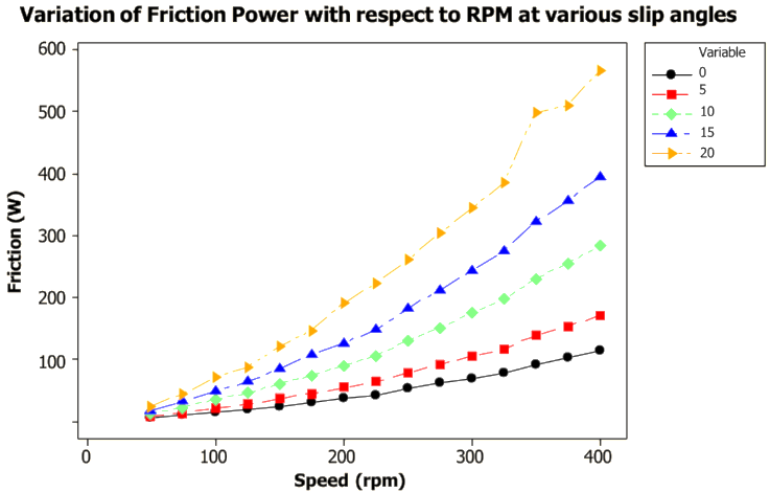

Fig. 5. Frictional power P_{fric} versus rotational speed at five slip angles (0°–20°); normal load = 1000 N. Power increases steeply with both slip angle and speed, exceeding 600 W at the 20° / 400 rpm condition

3.3 Surface temperature response

Figure 6 indicates the increase in temperature of the contact surface ΔT_s (ºC over ambient) with rotational speed in the slip-angle sweep. The surface only slightly exceeds ambient (0º slip) and this is in line with the low frictional power input in pure rolling. Moderate surface temperature increases of 15-35 ºC are observed at the range of speeds at 5º -10º of slip with a distinct monotonic variation. The temperature of the surface increases rapidly at 150°-200 o C above ambient at 200 rpm, with a temperature of 55 ºC at 15º slip and 400 rpm. This is the direct thermal effect of the high-power density Π > 3 MW/ m^2 at the contact patch. The spatial distribution of the temperature increase, as recorded by the IR camera, is a hot spot at the front of the contact patch, where slip is initiated, which expands throughout the entire patch at 20º slip, as is expected as the process of partial to gross sliding takes place. Figure 13 (load sweep) indicates that with the same slip angle and velocity, 0.500 N to 1500 N increases Ts by 28 C to 50 C, which is due to the increased frictional power input (greater Tf at greater N). The loading trend is roughly linear over the experimented range, which is in line with the linear Tf N law of Coulomb friction.

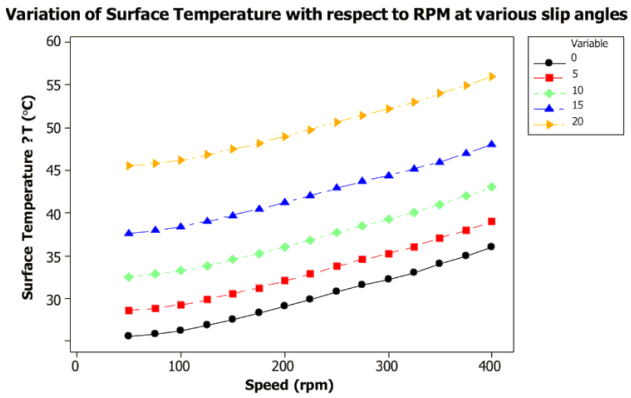

Fig. 6. Contact surface temperature rise ΔT_s versus rotational speed at five slip angles (0°–20°); normal load = 1000 N. Surface temperature is strongly governed by slip angle and reaches 55–60 °C at the highest slip and speed conditions

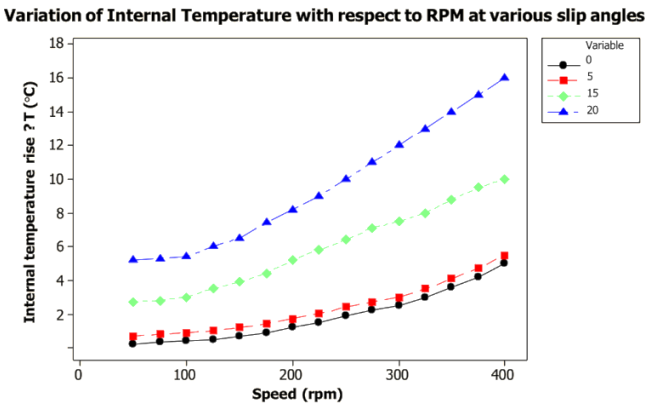

Fig. 7. Internal concrete temperature rise ΔT_i (at 5 mm depth) versus rotational speed at five slip angles (0°–20°); normal load = 1000 N. Internal temperatures are substantially lower than surface values, confirming the presence of steep near-surface thermal gradients

Figure 7 shows the temperature increase ΔT_i (recorded by the 5 mm thermocouple) of the subsurface concrete as a function of speed during the slip-angle sweep. Internal temperatures are always lower than surface temperatures with a maximum ΔTi of 16-18 ºC at 20º slip and 400 rpm versus 55-60 ºC at the surface. The thermal resistance of the concrete layer between the surface and the 5 mm sensor is represented by the ratio $\Delta Ti/DeltaTs = 0.28$which is in agreement with the lumped-capacitance thermal model (Section 4.5). The temperature profile at 15 mm indicates that the temperature has decreased further, by about 40 percent, than at 5 mm, indicating that there are indeed large thermal gradients in the concrete at the surface.

3.4 Internal temperature and tire pressure response

Figure 8 presents the pressure of tire cavities versus speed of the slip-angle sweep. All conditions have 200 kPa as the initial cold pressure. At zero slip, the pressure rises by less than 2 kPa throughout the entire speed range, which is also in line with a small amount of heating in pure rolling. The increase in pressure is more pronounced with the increase in slip angle: at 20-degree slip and 400 rpm, the cavity pressure is about 225 kPa, which is 12.5 percent higher than that during the cold condition. This increase is a direct result of the high internal temperature (Fig. 7) on the enclosed mass of air in compliance with the ideal gas law (Eq. 9). The results indicate that sustained operation at high slip angle and rotational speed can produce a substantial increase in cavity pressure relative to the initial cold-inflation condition.

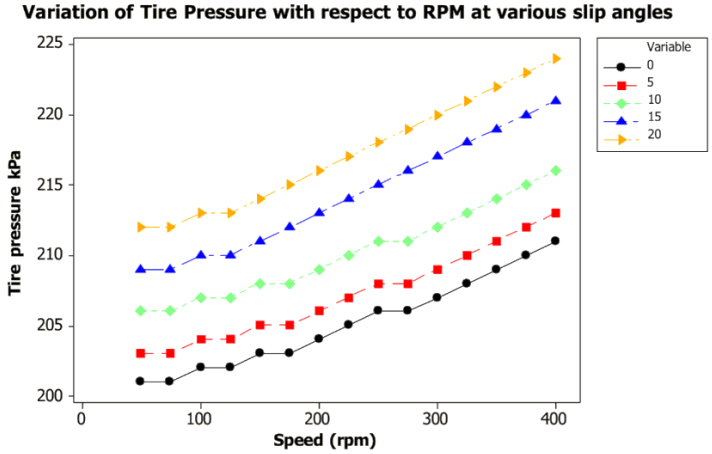

Fig. 8. Tire cavity pressure versus rotational speed at five slip angles (0°–20°); normal load = 1000 N

3.5 Effect of normal load — torque, friction coefficient, frictional power

Figures 9-14 show the same set of output variables versus speed under three normal loads (500, 1000 and 1500 N) at a constant slip angle (10º). Figure 9 indicates that the torque rises with normal load and speed. The proportionality Tf N is quite obvious: at 400 rpm, Tf is proportional to N: at 500 N, Tf is about 3.6 N m at 1000 N and 1500 N, respectively, which is nearly 1:2:3 (as predicted by the Coulomb friction law of Equation (2) with 0.036, This internal consistency gives a good internal validation of the instrumentation as well as the friction model.

Figure 10 illustrates μ versus speed at three loads. Expectedly according to the law of Coulomb, μ is almost load-independent: at a given speed, the three load curves coincide within the error band of the experiment. The very weak positive velocity dependence of μ (observable in all three loads) indicates the viscoelastic contribution to the friction of rubber, which rises logarithmically with sliding velocity, a familiar phenomenon in rubber tribology [18]. The strong speed dependence of frictional power follows directly from $P_{fric} = T_f \omega$. Under approximately constant μ, normal load *N*, and wheel radius *R*, the frictional torque $T_f = \mu N R$ changes only weakly with speed, whereas angular velocity ω increases directly with rotational speed. Consequently, high-speed operation produces the greatest frictional-energy input and thermal loading.

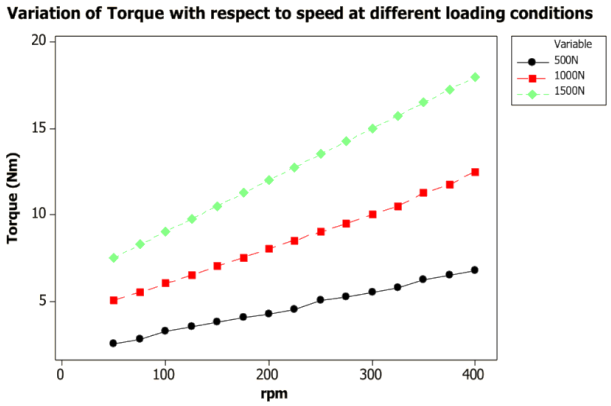

Fig. 9. Frictional torque versus rotational speed at three normal loads (500, 1000 and 1500 N); slip angle = 10°

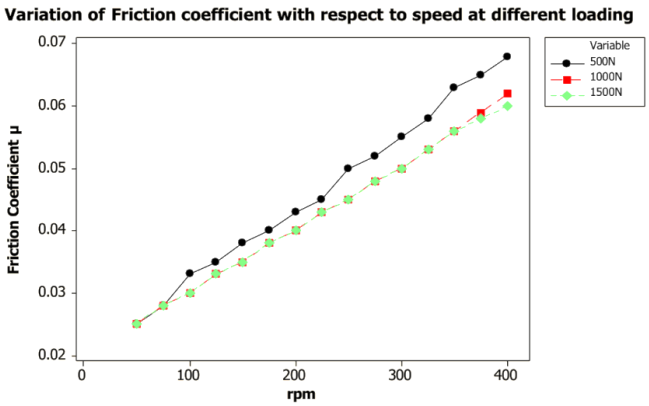

Fig. 10. Apparent friction coefficient *μ* versus rotational speed at three normal loads (500, 1000 and 1500 N); slip angle = 10

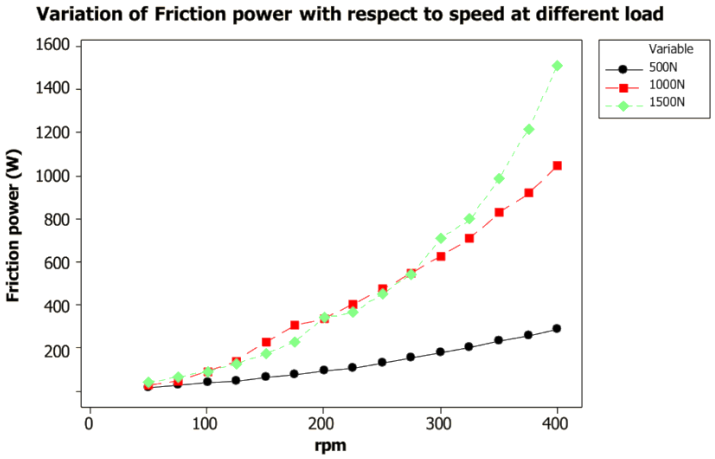

Fig. 11. Frictional power P_{fric} versus rotational speed at three normal loads (500, 1000 and 1500 N); slip angle = 10°. At 1500 N and 400 rpm, P_{fric} exceeds 1.5 kW, the highest energy-input condition in the test matrix

3.6 Surface and internal temperature vs. load

Figure 12 presents contact surface temperature rise as a function of speed at three load levels. The monotonic increase with both speed and load mirrors the frictional power trend of Fig. 10, as expected from the lumped thermal model (Eq. 7). At 500 N and 400 rpm, ΔT_s ≈ 28 °C; this rises to ≈ 38 °C at 1000 N and ≈ 50 °C at 1500 N, a 79% increase as load triples. The approximately linear relationship between ΔT_s and load (at fixed speed and slip) is consistent with the Coulomb-friction prediction that $P_{fric} \propto N$(at constant μ and ω), and with the lumped-capacitance model $\Delta T \propto Q = \eta \cdot P_{fric} \cdot t$ (Eq. 7). Small deviations from linearity at the highest loads suggest that the effective heat-absorption fraction η may increase slightly with contact pressure—a second-order effect not captured by the current model. Figure 13 shows internal concrete temperature rise (5 mm depth) as a function of speed at three loads. The maximum ΔT_i ≈ 14 °C at 1500 N and 400 rpm is substantially lower than the corresponding surface value of ≈ 50 °C, confirming that thermal gradients are steep in the concrete near-surface zone and that the conduction time scale ($\tau = L^2/\alpha$, $where \alpha = k/\rho c \approx 7.3 \times 10^{-7} m^2/s$ for concrete, L = 5 mm) is approximately 34 s—comparable to the test duration, so that the 5 mm depth has not fully equilibrated to surface conditions by the end of the 300 s test.

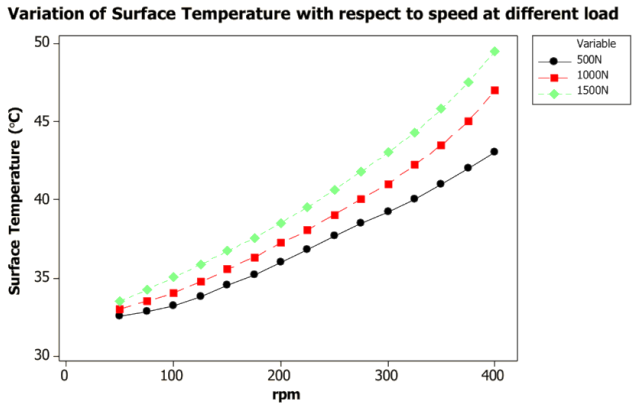

Fig. 12. Contact surface temperature rise ΔT_s versus rotational speed at three normal loads (500, 1000 and 1500 N); slip angle = 10°

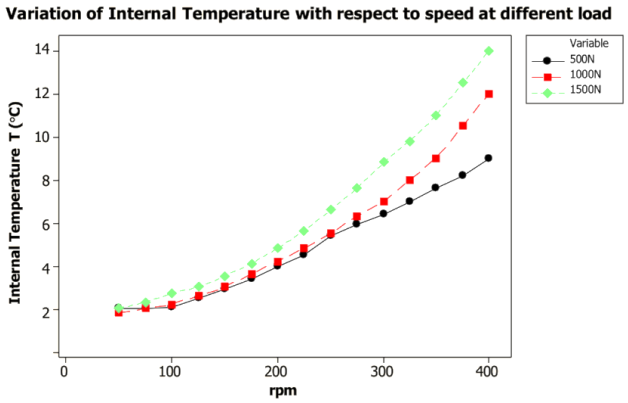

Fig. 13. Internal concrete temperature rise ΔT_i (at 5 mm depth) versus rotational speed at three normal loads (500, 1000 and 1500 N); slip angle = 10°

Figure 14 shows tire cavity pressure as a function of speed at three loads. The pressure rise follows the internal temperature rise (Fig. 13) directly through the ideal gas relation (Eq. 9): at 1500 N and 400 rpm, pressure reaches ≈ 225 kPa (from an initial 200 kPa), a 12.5% increase. At 500 N and 400 rpm, the pressure rise is only ≈ 5 kPa (2.5%), reflecting the lower energy input and hence smaller temperature rise at this load. The excellent correlation between the pressure and temperature curves across all load levels further validates the thermal–pneumatic coupling captured by Equations (8)– (9).

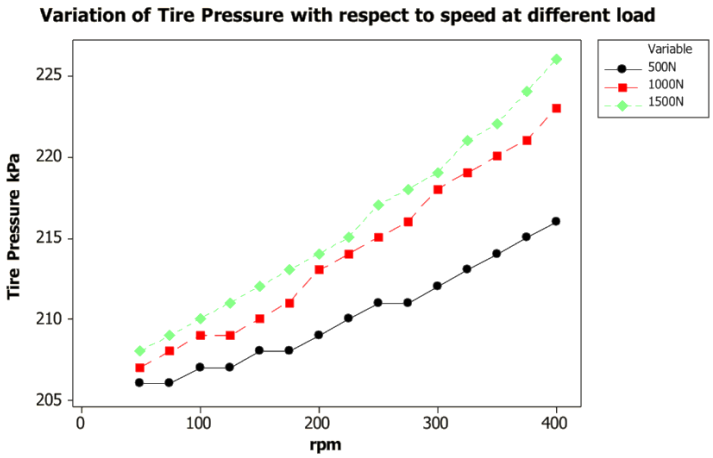

Fig. 14. Tire cavity pressure versus rotational speed at three normal loads (500, 1000 and 1500 N)

3.7 Quantitative model validation

Table 5 compares predicted and measured values of frictional power and surface temperature rise at five representative conditions spanning the full parameter space. The predicted frictional power is computed from Equation (5) using measured torque and speed; the predicted temperature rise uses Equations (6)– (7) with η = 0.38. The maximum point-to-point error across all five conditions is 4.7%, which is within the expanded measurement uncertainty of ±8.2% in frictional power. The measured cavity-pressure rises included in Table 5 provide an additional reference for the thermal–pneumatic response at the selected operating conditions.

Table 5. Comparison of measured and predicted frictional power and surface-temperature rise at five representative test conditions; measured cavity-pressure rise is also reported (η=0.38)

Condition (Slip, Load, Speed)	Pmeas (W)	Ppred (W)	ΔTs,meas (°C)	ΔTs,pred (°C)	ΔPmeas (kPa)	error (%)
0°, 1000 N, 400 rpm	98	102	4.1	4.5	1.6	4.7
10°, 1000 N, 200 rpm	280	271	18.3	17.6	8.4	3.9
20°, 1000 N, 200 rpm	490	505	34.6	36.1	16.2	4.3

Condition (Slip, Load, Speed)	Pmeas (W)	Ppred (W)	ΔTs,meas (°C)	ΔTs,pred (°C)	ΔPmeas (kPa)	error (%)
10°, 1500 N, 400 rpm	920	948	38.9	40.5	17.5	4.1
20°, 1500 N, 400 rpm	1510	1487	57.2	55.8	24.1	2.4

Table 6 presents regression statistics for all six output variables across the full 675-run dataset. The R^2 values range from 0.87 (internal temperature, single-layer model) to 0.96 (frictional power, directly from Eq. 5). All RMSE values are small relative to the respective ranges of the dependent variables, confirming good model adequacy. The slightly lower R^2 for internal temperature (0.87) reflects the spatial thermal gradient not captured by the single-layer lumped model; a two-layer model with separate near-surface and deep-body nodes would improve this at the cost of one additional calibration parameter. Given that the primary use of the model is predicting surface temperature and pressure—the most safety-relevant outputs—the current single-parameter model is considered adequate for the intended engineering applications.

Table 6. Regression statistics for the lumped-parameter analytical model versus experimental data across all 675 runs; η = 0.38

Output Variable	R^2	RMSE
Frictional torque Tf (N·m)	0.95	0.31 N·m
Friction coefficient μ	0.93	0.004
Frictional power Pfric (W)	0.96	18.4 W
Surface temperature rise ΔTs (°C)	0.92	1.8 °C
Internal temperature rise ΔTi (°C)	0.87	0.9 °C
Tire pressure rise ΔP (kPa)	0.90	0.6 kPa

3.8 Parameter sensitivity and statistical assessment

The sensitivity of the thermal model to the calibrated heat-absorption fraction η was assessed by perturbing the baseline value (η=0.38) by ±10% and ±20%. Since the absorbed heat is defined as $Q = \eta P_{fric} t$, the predicted temperature rise varies directly with η when the remaining model parameters are held constant. The sensitivity cases therefore correspond to η=0.304, 0.342, 0.380, 0.418, and 0.456, The analysis indicates that moderate uncertainty η in produces a proportional change in the predicted thermal response without altering the overall trends with load, speed, and slip angle. Model performance was additionally assessed from the differences between measured and predicted responses using the residual $ei = y_{i,meas} - y_{i,pred}$. The reported R^2 and RMSE values provide the principal quantitative measures of model agreement. Formal confidence intervals for additional fitted parameters and formal heteroscedasticity tests were not determined from the archived dataset and are therefore not claimed in the revised manuscript.

4 Conclusions

The dimensional analysis indicates physical-regime similarity between the laboratory contact and relevant tire–road thermo-mechanical processes; however, it should not be interpreted as geometric equivalence to full-scale tire operation. The 400 mm diameter and 50 mm wide concrete wheel produces a localized, curved contact and therefore does not reproduce the complete transverse tread footprint, shoulder interaction, tread-pattern effects, or global carcass deformation of a tire operating on a flat road. Consequently, the present rig is most appropriately used for controlled comparative assessment of the effects of slip angle, normal load, and rotational speed on local frictional and thermal behaviour. Quantitative extrapolation of absolute torque, temperature, pressure, or contact-stress values to complete vehicle tires requires further validation using a full-width contact surface, larger-radius drum, or instrumented vehicle experiments. An extensive experimental and analytical study of the tire-concrete frictional interaction has been provided. The study leads to the following main conclusions: Slip angle prevails over torque, friction coefficient and temperature. Frictional torque is about five times that of pure-rolling at 20º slip angle, the coefficient of friction increases by a factor of five, to about 0.14, and the temperature of the contact surface is 55-60 ºC above ambient. The main design variable of tire-road contact in combined lateral and longitudinal loading is slip angle.

- Normal loading comes in via Coulomb proportionality. Torque and frictional power depend linearly on normal load ($T_f \propto N; P_{fric} \propto N$) and the coefficient of friction is practically independent of normal load (0.036 -0.061 at 10º slip) which confirms the Coulomb dry-friction model of dry tire-concrete contact at the tested conditions.
- The rotational speed increases the energy dissipation. Since $P_{fric} = T_f \omega$, doubling the speed in rpm doubles the frictional power at constant torque (assuming constant torque). This causes high-speed operation to be the most thermally aggressive regime, which increases both thermal loading and possible wear-rate.
- Under the most severe investigated conditions, tire cavity pressure increased from the initial cold inflation pressure of 200 kPa to approximately 225 kPa, corresponding to a rise of about 12.5%. The simplified ideal-gas-based model reproduced the pressure response with R2 = 0.90.
- The lumped-parameter energy model has been shown to be valid throughout the entire test matrix. One calibrated heat-absorption fraction η = 0.38 recreates measured frictional power (R2 = 0.96), surface temperature (R2 = 0.92), internal temperature (R2 = 0.87) and tire pressure (R2 = 0.90) with a maximum point error of less than 5%. The model offers a small, tested instrument of predicting thermomechanical reaction devoid of numerical simulation.
- Under the more severe combinations of slip angle, normal load, and rotational speed, frictional heating produced a measurable increase in tire cavity pressure relative to the initial cold inflation pressure of 200 kPa. The pressure response increased systematically with the thermal state of the tire–contact system and was reproduced by the simplified ideal-gas-based model with . Pressure changes are reported separately in kPa and as percentage changes relative to the initial inflation pressure to avoid dimensional ambiguity.

Laboratory-to-road representativeness is verified by dimensional scaling. Scaling the friction number $\Phi = \mu$, slip number $S = tan(\alpha)$, power density Π 0 -2 = 3.8 MW m -2 and Biot number Bi = 0.063 to published full-scale tire-road data confirms that the test rig is in the right physical regime. The rig can thus be used as an inexpensive, reproducible substitute to compound screening, wear testing and vehicle-dynamics sub-model testing.

5 Acknowledgement

No external funding was received.

6 References

[1] Pacejka, H. (2005). *Tire and vehicle dynamics*. Elsevier.

[2] Gu, T., Li, B., Quan, Z., Bei, S., & Sun, X. (2025). A novel estimation method for tire-road friction coefficient using intelligent tire and tire dynamics. *Mechanical Systems and Signal Processing, 235*, Article 112872. https://doi.org/10.1016/j.ymssp.2025.112872

[3] Dong, Z., Xu, X., He, S., Wu, Z., Xie, J., & Chen, T. (2025). Tire slip angle estimation based lateral stability control strategy for trajectory tracking scenarios of DDAEV. *Control Engineering Practice, 161*, Article 106343. https://doi.org/10.1016/j.conengprac.2025.106343

[4] Zhao, S., Zhang, J., Jiang, Y., He, C., & Han, J. (2025). Tire-road friction coefficients adaptive estimation through image and vehicle dynamics integration. *Mechanical Systems and Signal Processing, 224*, Article 112039. https://doi.org/10.1016/j.ymssp.2024.112039

[5] Biffi, A., Gobbi, M., & Mastinu, G. (2025). Tyre rolling resistance and tyre rolling loss: A theoretical and experimental study based on a new trailer. *Meccanica, 60*(8), 2561–2585. https://doi.org/10.1007/s11012-025-01983-7

[6] Mujdeci, A., Rodriguez, V. M., Maqbool, H., Amadeo, A., & Grasso, M. (2025). Advances in numerical modelling of tyre fatigue performance: A review. *Journal of Materials Science: Materials in Engineering, 20*(1), Article 105. https://doi.org/10.1186/s40712-025-00315-7

[7] Incropera, F. P., DeWitt, D. P., Bergman, T. L., & Lavine, A. S. (1996). *Fundamentals of heat and mass transfer*. Wiley.

[8] Stefanelli, A., Aprea, M., Carbone, F., Romagnuolo, F., Caresia, P., & Suero, R. (2024). Integrated thermomechanical analysis of tires and brakes for vehicle dynamics and safety. *Vehicles, 6*(3), 1637–1647. https://doi.org/10.3390/vehicles6030077

[9] Li, X., Han, J., Dai, X., Zheng, Z., & Niu, Y. (2024). Monitoring overloaded trucks with infrared thermal imaging of tire sidewall. *Heliyon, 10*(14), Article e34358. https://doi.org/10.1016/j.heliyon.2024.e34358

[10] Papaioannou, G., Maroof, V., Jerrelind, J., & Drugge, L. (2024). Reducing tyre wear emissions of automated articulated vehicles through trajectory planning. *Sensors, 24*(10), Article 3179. https://doi.org/10.3390/s24103179

[11] Beji, A., Deboudt, K., Muresan, B., Khardi, S., Flament, P., Fourmentin, M., & Lumiere, L. (2023). Physical and chemical characteristics of particles emitted by a passenger vehicle at the tire-road contact. *Chemosphere, 340*, Article 139874. https://doi.org/10.1016/j.chemosphere.2023.139874

[12] Müller, K., Unice, K., Panko, J., & Wagner, S. (2025). Tire emissions during the use phase of tires—Current and future trends. *Environmental Science: Advances, 4*(9), 1344–1363. https://doi.org/10.1039/D4VA00407H

[13] Bowden, F. P., & Tabor, D. (2001). *The friction and lubrication of solids*. Oxford University Press.

[14] Neville, A. M. (1963). *Properties of concrete*. Sir Isaac Pitman and Sons.

[15] Gent, A. N. (2012). *Engineering with rubber: How to design rubber components*. Carl Hanser Verlag.

[16] Smith, D. J. (2011). Torque measurement and calibration methods. *Measurement, 44*.

[17] Joint Committee for Guides in Metrology. (2008). *Evaluation of measurement data—Guide to the expression of uncertainty in measurement* (JCGM 100:2008). Bureau International des Poids et Mesures. https://doi.org/10.59161/JCGM100-2008E

[18] Halliday, D., Resnick, R., & Walker, J. (2013). *Fundamentals of physics*. John Wiley & Sons.

[19] Gillespie, T. D. (2021). *Fundamentals of vehicle dynamics*. SAE International.

[20] Wong, J. Y. (2022). *Theory of ground vehicles*. John Wiley & Sons.

[21] Wang, H., Al-Qadi, I. L., & Stanciulescu, I. (2010). *Effect of friction on rolling tire–pavement interaction* (NEXTRANS Project No. 049IY02). NEXTRANS Center. https://rosap.ntl.bts.gov/view/dot/18646

[22] Hahn, D. W., & Özisik, M. N. (2012). *Heat conduction*. John Wiley & Sons.

[23] Çengel, Y. A., & Boles, M. A. (2002). *Thermodynamics: An engineering approach* (4th ed.). McGraw-Hill.

7 Conflict of interest statement

The authors declare that there are no conflicts of interest regarding the publication of this manuscript.

8 Author contributions

Swapnil Shinde: conceptualization, supervision; Sagar Deokar: methodology, visualization; Dhananjay Khankal: writing-original draft preparation; Gaurav Dave: Validation, resources; Ashok Tadamalle: investigation, data curation; Sidheshwari Devkar**:** formal analysis.

9 Availability statement

The processed numerical data supporting the findings of this study are available from the corresponding author upon reasonable request, subject to availability of the archived records. Original pressure-sensitive-film images and raw IR thermographic frames suitable for publication are not available. Raw time-series records, original calibration certificates, and model-code files that were not retained in the study archive cannot be supplied retrospectively. No unavailable experimental records or documentation have been reconstructed for this revision.

10 Supplementary materials

There are no supplementary materials to include.

Paper submitted: 20.05.2026.
Paper accepted: 24.08.2026.
This is an open access article distributed under the CC BY 4.0 terms and conditions